Ceramics International 51 (2025) 48878–48888

Contents lists available at ScienceDirect

Ceramics International

journal homepage: www.elsevier.com/locate/ceramint

A supersaturated glass-melt approach for growing micrometer-sized TGG single crystals

Juliane Resges Orives [a], Thiago Augusto Lodi [a], Lia Mara Silva Marcondes [b], Camila Batista Pinto [c], Victória Mamelli [a], Antonio Eduardo Souza [a], Fabricio Benedito Destro [a], Juliani Caland [d], Javier Alcides Ellena [c], Thierry Cardinal [b], Marc Dussauze [e], Jorlandio Felix [d], Marcelo Nalin [a,*]

[a] Institute of Chemistry, São Paulo State University (UNESP), Araraquara, SP, Brazil
[b] Institut de Chimie de la Matière Condensée de Bordeaux, Université de Bordeaux, 87 Avenue du Dr Schweitzer, F-33608, Pessac, France
[c] São Carlos Institut of Physics (IFSC), University of São Paulo (USP), São Carlos, SP, Brazil
[d] Institute of Physics, Applied Physics Center, University of Brasília, Brasília, DF, 70919-970, Brazil
[e] Institut des Sciences Moléculaires, UMR 5255, Université de Bordeaux, 351 cours de la Liberation, 33405, Talence Cedex, France

ARTICLE INFO

Handling Editor: Dr P. Vincenzini

Keywords:
Terbium gallium garnet
Melt-quenching
Heavy metal oxide glasses
Glass ceramics
Single crystals

ABSTRACT

Terbium gallium garnet (TGG, $Tb_3Ga_5O_{12}$) is an important material used as Faraday rotator in telecommunication, in interferometric facilities and in other important technological and photonic applications. TGG can be synthesized using different methodologies, however obtaining single crystals on a large scale is still a challenge. In this paper, for the first time, micrometric cubic single crystals were obtained from rare earths supersaturated melted heavy metal oxide glass compositions. A systematic study of the glass composition allied to the control of cooling parameters allowed the synthesis of micro-scale single crystals. A chemical route is proposed to isolate the crystals from the parent glass without compromising their properties. A series of structural and spectroscopic techniques was employed to characterize the crystals, which crystallize in the Ia $\overline{3}$ d space group. XRD, Raman and EDS measurements demonstrate the formation of the $Tb_3Ga_5O_{12}$ crystalline phase and the microscopy images show the presence of microcrystals with a perfect cubic shape and size between 50 and 100 μm. Luminescence analysis indicates a green emission between 530 and 560 nm characteristic of the $^5D_4 \rightarrow {}^7F_5$ transitions of Tb^{3+} ions and the presence of Stark components as well resolved multiplets and perfectly coherent with the Stark components of the TGG crystal. Finally, SQUID measurements were performed on glass samples containing crystals and on isolated crystals after removal of the glass and both presented paramagnetic behavior. The effective magnetic moment obtained for the TGG microcrystals between 50 and 70 μm removed from the glass was 9.7 μB, the same value as the theoretical effective magnetic moment for Tb^{3+} ions. This achievement represents an advance in the methodologies for obtaining TGG cubes in the micro-scale range, opening the possibility of mass production of such crystal and its uses in different technological photonic applications.

1. Introduction

The development of lanthanide contend materials with photonic properties is essential to address the main current challenges in applications such as scintillators [1], luminescent thermometry [2–4], light emitting diodes [5,6], magneto-optical [7] and magneto-luminescent devices [8], among others.

Special ceramics, such as those based on garnets, have attracted attention in many recent applications. Among the garnets, those based on aluminum and gallium are applied in many of the applications mentioned above. $RE_3Ga_5O_{12}$ and $RE_3Al_5O_{12}$ (RE = rare earth) garnet crystals in glass matrices have recently been highlighted due to their important fundamental and technological properties. Among the garnet-type crystals, the terbium gallium garnet ($Tb_3Ga_5O_{12}$, TGG) is the single crystal most used commercially as a Faraday rotator device due to its high Verdet constant [9]. In addition to its magnetic and

* Corresponding author. Instituto de Química, Universidade Estadual Paulista Júlio de Mendonça Filho – UNESP, Rua Prof. Franscisco Degni, 55, Quitandinha, Araraquara, SP, CEP 14800-060, Brazil.
E-mail address: marcelo.nalin@unesp.br (M. Nalin).

https://doi.org/10.1016/j.ceramint.2025.08.137
Received 4 June 2025; Received in revised form 1 August 2025; Accepted 10 August 2025
Available online 11 August 2025

magneto-optical properties, TGG has excellent optical quality, it is mechanically hard, chemically stable, and has interesting luminescent properties since the Tb^{3+} ion exhibits green emission near 544 nm due to the $^5D_4 \rightarrow {}^7F_5$ transition [9–15]. TGG can be obtained in different formats, such as single crystals [12], nano-powders [16], polycrystalline ceramics [17], and bulk [18]. Several synthesis methods have been reported, for example, metal-organic decomposition [19], micro-pulling-down [20], floating-zone [21], high-temperature solid--state method [22], co-precipitation [16], and the most popular Czochralski method [23–25].

Despite the various synthesis methods, production in a large scale faces some difficulties such as low quality of the crystal, significant long time for crystal growth and high cost to manufacture [26]. In this way, due to the large possibilities for TGG applications, the need to find new methodologies of obtaining these single crystals remains in focus [26]. The synthesis of new glass compositions, as well as the advances in understanding of the chemistry of their formation, allows us to obtain compositions where the formation of crystals in the glass phase can be controlled. The glass materials have a structure similar to its original super-cooled liquid, and one of its most interesting properties is the possibility of dispersing other chemical elements in its composition, such as, for example, metal or rare-earths ions, and then, it is possible to grow nanocrystals and microcrystals in the glass matrix by controlled thermal treatment [27–30]. In addition to being able to explore the properties of glass ceramics, there is also the possibility of removing crystals from the glass matrix, which has not yet been explored in literature. This approach could generate a wide range of applications.

Heavy metal oxide glasses can be a good alternative for obtaining single crystals of TGG, as they are materials that are easy to obtain on a large scale, they have important properties such as large window transparency from the visible up to medium infrared region, low phonon energy, high refractive index, and good chemical stability, among others [30]. The growth of TGG single phase within a glassy matrix is a complicated task. The main challenge is to obtain a glass with good optical properties, with crystals having active terbium ions within the crystalline phase distributed in a homogeneous way in the matrix. Furthermore, in multicomponent compositions, other phases, in addition to TGG, can also be obtained. Promising results of obtaining Er^{3+}/Tm^{3+}- doped cubic $Yb_3Ga_5O_{12}$ single-crystals dispersed in a germano-gallate glass system were presented by Souza et al. [30] showing that it would be possible to obtain the TGG crystal once the two crystals belong to the same garnet family.

The synthesis of crystals in glasses can occur by heat-treating the sample above glass transition temperature or from the melt of glass precursors at high temperatures followed by controlled cooling to induce nucleation and consequently crystal growth [27–29]. Crystallization from the melt is a complex process that requires the formation of supersaturated solutions, since a new phase can be precipitated only when a system is in a non-equilibrium condition, followed by the aggregation of dissolved ions to relieve the supersaturation allowing the system to move toward equilibrium [31]. Both composition and cooling rate conditions have an important role in determining the structural phase and size of the resulting crystals. Furthermore, uniform nucleation and growth are important to have crystals distributed throughout the glass volume [31].

In this context, the objective of this work was to synthesize micrometric TGG single crystals embedded in heavy metal oxide glass in an easy, controlled and reproducible way. Furthermore, a method for extracting the crystals from the glass matrix is demonstrated. A systematic study of the structural, morphological, optical, luminescent and magnetic properties of glass ceramics and single crystals is also presented.

2. Experimental

2.1. Glass ceramics preparation and crystal isolation

Multicomponent heavy metal oxide bulk glasses with molar composition $40PbO\text{-}25Bi_2O_3\text{-}20GeO_2\text{-}15Ga_2O_3$ and $98.5(40PbO\text{-}25Bi_2O_3\text{-}20GeO_2\text{-}15Ga_2O_3)\text{-}1.5Tb_4O_7$ were studied. The following analytical grade raw materials were used: GeO_2 (99.999 %), Ga_2O_3 (99.99 %) and Bi_2O_3 (99.975 %) from Alfa Aesar, PbO (99.0 % - Fluka), Tb_4O_7 from REEtec (99.96 %). To control the quantity and the size of crystals obtained, two methodologies were used. The first consists of pouring the melt into the mold by melt-quenching process at different times and the second carried out by controlled cooling of the melt inside the furnace. In the first case, the raw materials were melted at 1250 °C for 2 h for full homogenization. Then, samples containing terbium were stirred at 0, 2, 3 and 4 s before being poured into a steel mold preheated at 350 °C and labeled as (PGBG-Tb-0), (PGBG-Tb-2), (PGBG-Tb-3) (PGBG-Tb-4) (Fig. S1 in the supplementary information), respectively. The sample without terbium was labeled as PGBG. The glasses were polished with sandpapers for improving their optical quality. In the second case, the precursors were melted at 1250 °C for 2 h for full homogenization and then the furnace was set to cool down at a rate of 10 °C/min until reaching 900 °C, then the sample was removed from the furnace at this temperature. To extract the crystals, the glass ceramic was immersed into concentrated nitric acid during 24 h. Finally, after dissolving the glass material, the crystals were washed with distilled water several times and dried in an oven at 100 °C.

2.2. Characterization techniques

Optical images were collected using an optical microscope Leica DM2500M model. The UV–Vis absorption spectra (in the spectral range from 450 to 2500 nm) were recorded using a Varian Cary 5000 UV–Vis–Near infrared (NIR) spectrophotometer, on the polished samples of 1.5 mm thickness. Micro-luminescence data was acquired using a Labram (Horiba) spectrometer with a laser source at 488 nm, a 150 nm grooves grating and 50X (N.A. = 0.54) objective. Then, micro-Raman was acquired from a spectrometer HR800 (Horiba/Jobin Yvon) with a 100X (N.A. = 0.9) objective with a CW laser operating at 532 nm. The X-ray powder diffraction of PGBG-Tb-4 sample was carried out with a Bruker D8 Advance diffractometer operating with a Ni filtered CuKα radiation source at 2θ angle ranging from 10 to 80° with a step pass of 0.02° and a step time of 2 s. Scanning electron microscopy images, Energy-dispersive X-ray spectroscopy (EDS) and elemental mapping were obtained with a microscopy JEOL-SJSMT-IT500HR. The crystals were carbon-coated to about 5 nm thickness using a Sample Sputter Coater SCD 050™ (Bal-Tec, Wallruf, Germany). X-ray data collection for the single crystal was performed on a XtaLAB Synergy-S Dualflex diffractometer, equipped with a HyPix-6000HE detector and microfocus sealed tube X-ray source. Data was collected at 100 K using Mo *Kα* radiation (λ = 0.71073 Å). Data collection, reduction and absorption correction were conducted with the CrysAlisPro software. The structure was solved with SHELXT 2018/2 program using the Intrinsic Phasing method and refined on F^2 with SHELXL 2019/2 through the full-matrix least-squares method, using *Olex2* [32] as graphical interface. The program VESTA [33] was used for preparation of graphics, as well as for calculations concerning the coordination centers. Further experimental details are found in Table 1.

Magnetization measurements have been carried out using a VSM-SQUID from Quantum Design PPMS3 with a DC field ranging from 70 to 70 kOe at 5 and 300 K. Temperature-dependent magnetic susceptibilities were studied under a magnetic field of 100 Oe and temperature ranging from 5 to 300 K. The diamagnetic correction was done from the undoped glass.

Table 1
X-ray experimental details for the single crystal.

Crystal data	
Chemical formula	$Tb_3Ga_5O_{12}$
M_r	1017.36
Crystal system, space group	Cubic, *Ia* $\bar{3}$ *d*
Temperature (K)	100
a (Å)	12.3539 (3)
V (Å^3)	1885.44 (14)
Z	8
Radiation type	Mo *K*α
μ (mm^{-1})	36.32
Crystal size (mm)	0.14 × 0.11 × 0.11
Data collection	
Diffractometer	XtaLAB Synergy, Dualflex, HyPix
Absorption correction	Gaussian Numerical absorption correction based on gaussian integration over a multifaceted crystal model. Empirical absorption correction using spherical harmonics, implemented in SCALE3 ABSPACK scaling algorithm.
T_{min}, T_{max}	0.062, 0.126
N° of measured, independent and observed [$I > 2\sigma(I)$] reflections	1740, 211, 196
R_{int}	0.039
(sin θ/λ)$_{max}$ (Å^{-1})	0.675
Refinement	
$R[F^2 > 2\sigma(F^2)]$, w$R(F^2)$, *S*	0.022, 0.060, 1.30
N° of reflections	211
N° of parameters	18
$\Delta\rho_{max}$, $\Delta\rho_{min}$ (e Å^{-3})	1.14, −0.85

3. Results and discussions

The 98.5(40PbO-25Bi_2O_3-20GeO_2-15Ga_2O_3)-1,5Tb_4O_7 composition was chosen based on a previous work reported by Nalin, M et al. [29], which has demonstrated the possibility of obtaining $Yb_3Ga_5O_{12}$ single crystals doped with Er^{3+}/Tm^{3+} in a germano-gallate glass system containing 3 mol% of rare-earths. However, in this paper, the concentration of 1.5 mol% of terbium oxide (Tb_4O_7) was sufficient to present the supersaturated condition for the formation of crystals from the glass melt.

Fig. 1a shows the photograph of the samples obtained and it is observed that with increasing stirring time, before pouring the melted glass into the steel mold, there is an increment in the opacity of the glass. In Fig. 1(b–e), it is possible to verify from the optical microscopy images that crystal formation occurred in all PGBG-Tb samples. These crystals, with size between 10 and 20 μm, are composed of smaller crystals forming polycrystals. The shape of this polycrystalline material is governed by the symmetry of the single crystals that compose it. In this manner, the shape of the polycrystals in Fig. 1b–e is related to the cubic crystal system, as described through X-ray diffraction techniques (see below). It is possible to observe a greater opacity in the sample as the stirring time increases which may have occurred due to a qualitative increase of crystals. For the PGBG-Tb-4 sample, it is possible to observe, in addition to the polycrystals, the formation of some cubic crystals with more defined faces, suggesting the formation of single crystals due to the longer time for organization of the structure.

The X-ray diffractogram of sample PGBG-Tb-4 shows a diffuse-halo of diffraction at 28° (Fig. S2 in the supplementary information), characteristic of amorphous glasses, which indicated that the amorphous state remains in the sample despite the large number of crystals observed microscopically. Furthermore, it presents the diffraction peaks at 28.9°, 32.3°, 35.5°, 53.3° and 59.7°, which were indexed to the

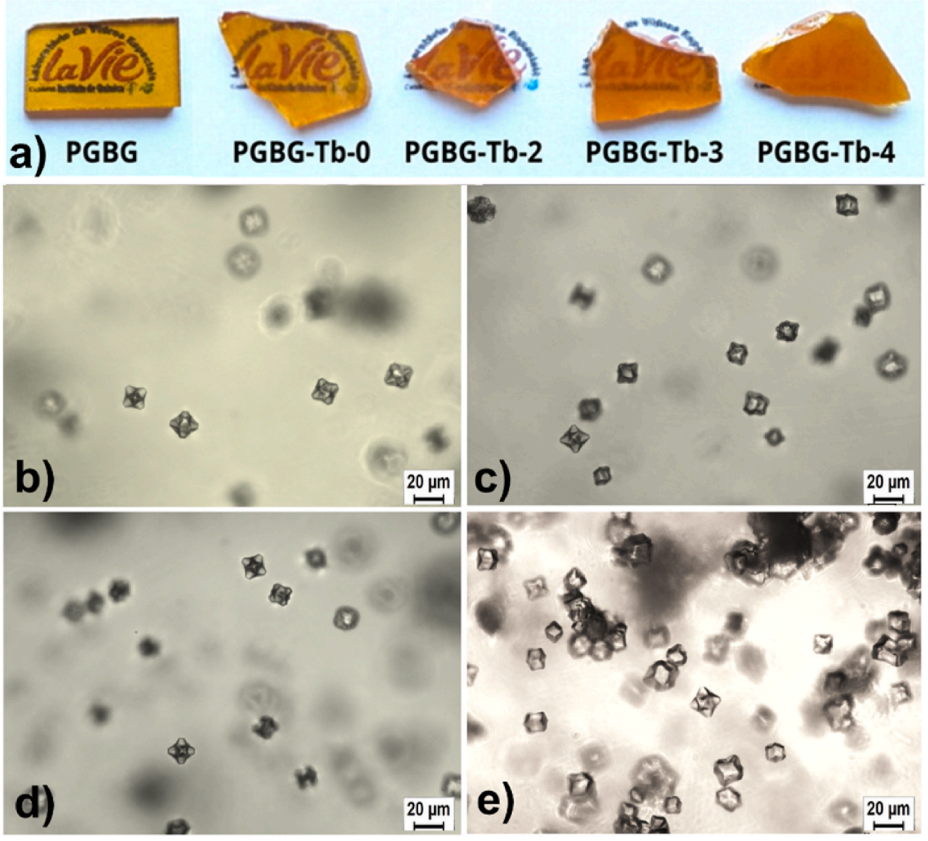

Fig. 1. **(a)** Photography of PGBG pristine glass and PGBG-Tb samples. Optical microscopy images of **(b)** PGBG-Tb-0, **(c)** PGBG-Tb-2, **(d)** PGBG-Tb-3 and **(e)** PGBG-Tb-4.

crystalline phase of $Tb_3Ga_5O_{12}$ that crystallizes in the cubic space group Ia-3d (ICSD-20831). The peaks were assigned to the planes 004, 420, 422, 046 and 080, respectively. These results confirm that the glass ceramic obtained is composed of the glass phase and the TGG crystals.

The optical absorption spectra of samples in UV–Vis–NIR wavelength range are shown in Fig. 2 (a). Several absorption bands would appear before 500 nm assigned to the transitions of Tb^{3+} ions, however, the f-f absorption bands are covered by the UV cut-off edge that limits the transmission window. The broadened bands originating from f-f transitions of Tb^{3+} ions are observed in the NIR range. In this region, bands around 1780, 1890, 1950 and 2215 nm appear due to transitions within ground state multiplets $^7F_6 \rightarrow {}^7F_0$, $^7F_1$, $^7F_2$ and $^7F_3$ levels of Tb^{3+} ions, respectively [34]. However, it could be noticed that, with the increase pouring time, the absorption bands become progressively more defined. Absorption band profile is modified due to a change of the magnitude and symmetry of the coordination sphere of the Tb^{3+} ions energy levels. This is because for samples where the pouring time is shorter, the rare earths are present in both glass and crystalline phases. However, absorption from amorphous structure, such as that of glass, leads to broader absorptions, since the environment around the rare earth is not homogenous in the atomic scale, and small changes in angles and bond distances can be expected [35]. Thus, for the first samples, the main emission coming from Tb^{3+} ions from glass phase. On the other hand, rare earth ions embedded into organized arrangements, such as those of the single crystals, present more defined emissions, arising from the so-called Stark levels. Thus, due also to greater crystal precipitation, presented in samples with longer pouring times, the emission bands are also more defined, such as those seen in Fig. 2e. In this perspective, one can suggest the Tb^{3+} ions are likely to occupy crystalline environments due to the lower number of symmetrical sites and lower degeneracy of

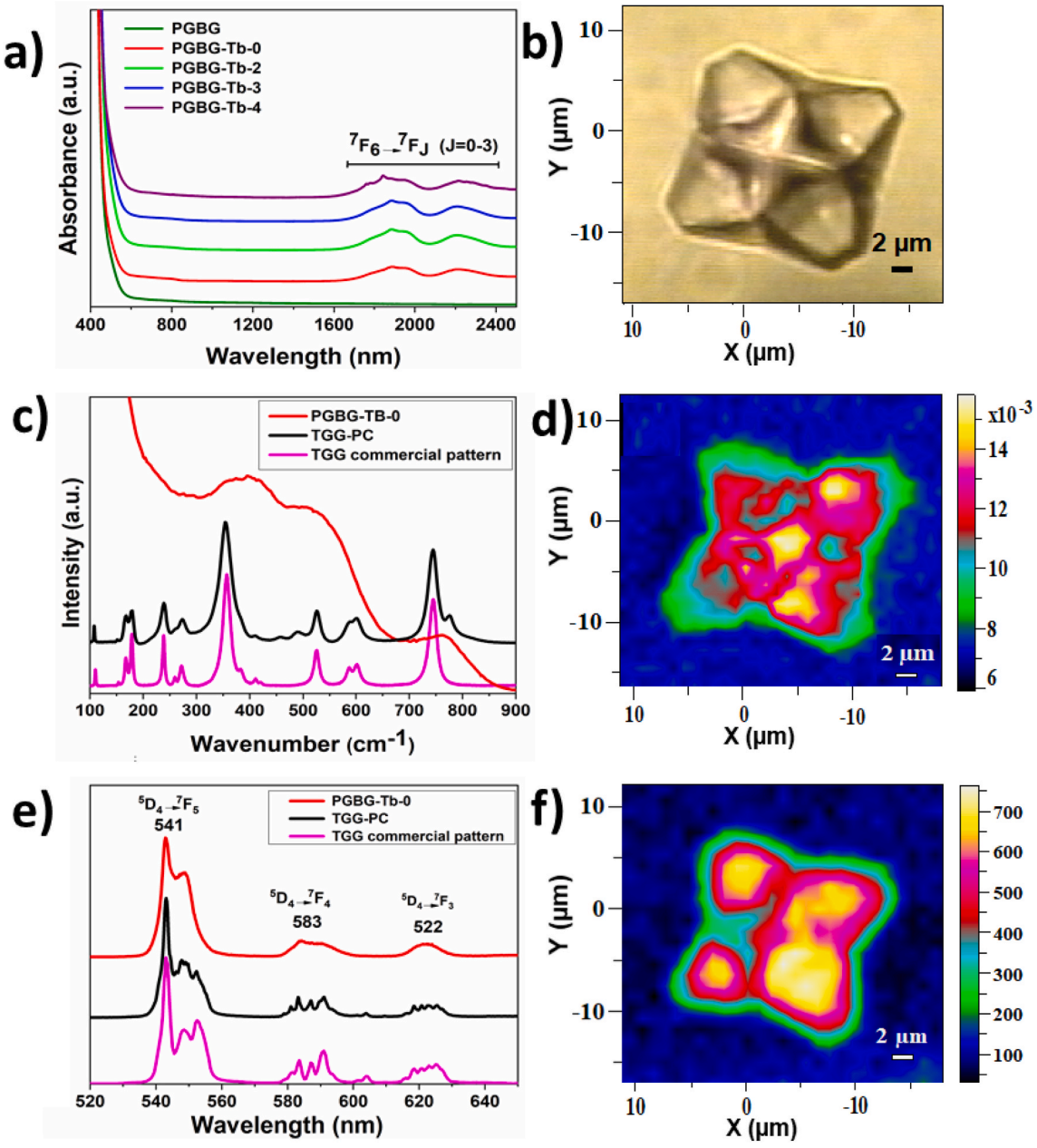

Fig. 2. **(a)** UV–Vis–NIR spectra obtained for PGBG and PGBG-TB samples (the spectra have been moved vertically for better viewing), **(b)** Optical microscopy image of a representative crystal of the sample PGBG-Tb-0, **(c)** Normalized Raman spectra acquired forPGBG-Tb-0 vitreous phase, TGG-PC and TGG commercial pattern, **(d)** micro-Raman map for band at 356 cm^{-1}, **(e)** Emission spectra acquired for PGBG-Tb-0 vitreous phase, TGG-PC and TGG commercial pattern and **(f)** Luminescence map for emission bands between 530 and 560 nm.

Tb^{3+} energy levels.

The structural changes were evaluated carrying out a micro-Raman experiment. For the measurement performed in the vitreous phase (PGBG-Tb-0), the spectra presented broad bands characteristic of a glassy material corresponding to the range of 300~800 cm^{-1} [30]. The bands in the regions around 380, 520 and 765 cm^{-1} are assigned to the vibration modes of Ge-O-Bi/Ga-O-Bi bonds, Ge-O-Ge or Ga-O-Ga bonds in GeO_4 or GaO_4 units and Ge-O- bonds involving non-bridging oxygen units, respectively [36,37]. In general, the glass network is composed of a germanate chain with GaO_4 polyhedra cross-linking the GeO_4 units [30]. Regarding crystallization, the micro-Raman spectra of the polycrystalline $Tb_3Ga_5O_{12}$ (TGG-PC) inside the glass and of a TGG crystal reference are presented in Fig. 2c. To complement the analysis and demonstrate the glass/crystal phase separation, a Raman cartography was collected (Fig. 2d). An area of ≅ 30 × 30 μm^2 was mapped with 1 μm step along X and Y axes. The map was generated for the band at 356 cm^{-1}, assigned to vibrational modes of GaO_6 units and shows the difference in composition between the glassy and crystalline part of the sample. The Raman bands for the TGG-PC inside the glass showed a profile very similar to the TGG crystal reference and the spectra reported in the literature for $RE_3Ga_5O_{12}$ structures [38–40]. The band assignments of this type of crystal analyzed by group theory are described by Monteseguro et al. [40].

To evaluate the luminescent properties of terbium ions in a glassy and crystalline environment, a micro-luminescence mapping was performed in a 30 × 30 μm^2 area using for excitation a 488 nm wavelength. The map was generated for emission bands between 530 and 560 nm (Fig. 2f). Two luminescence spectra (Fig. 2e) were extracted from the map one for PGBG-Tb-0 vitreous phase and other for TGG-PC region. Emission spectra were normalized at 547 nm, which is originated from the $^5D_4 \rightarrow {}^7F_5$ transitions. In addition to this green emission, yellow and red emission bands were observed at 587 and 624 nm and have been assigned to $^5D_4 \rightarrow {}^7F_j$ (J = 4 and 3) transitions of Tb^{3+} ions, respectively [9,10]. A qualitative comparison between the spectra shows the Stark splitting of Tb^{3+} ions energy levels in the spectrum of the TGG-PC sample in relation to the glassy part, suggesting that the Tb^{3+} ions are in chemical environments with a lower diversity of symmetry sites, which led to lower degeneracy of the Tb^{3+} energy levels. The emission spectrum from the commercial TGG crystal was obtained for comparison and corroborates the suggestion of the presence of terbium in TGG crystals precipitated in the glass matrix.

EDS and SEM measurements were collected and shown in Fig. 3. The signals obtained from EDS in the PGBG-Tb-0 glass area (1) in Fig. 3a were attributed to Ga at 0.95 (edge L1) and 1.098 keV (edge La1), to Ge at 1.19 keV (edge La1), to Bi at 2.42 keV (edge Ma12) and to Pb at 1.84 keV (edge Mx). The shoulder at 1.24 is attributed to Tb (Ec(M5)). The EDS results for TGG-PC area (2) shows that the chemical composition of crystals contains Tb with signals at 1.24 (Ec(M5)), 6.27 (edge La1), 6.97 (edge Lβ1) and 7.36 (edge Lβ2) and Ga with energies attributed at 0.95 (edge L1) and 1.098 keV (edge La1) (Fig. 3b). Fig. 3c shows first an SEM image of a crystal exposed on the glass surface and then the elemental mapping: Tb (signal at 6.27 keV), Ga (at 1.098 keV), Ge (at 1.19 keV), Pb (at 1.84 keV), Bi (at 2.42 keV). In the case of the elements Ge and Ga, they have close atomic numbers, thereby exhibiting similar transitions, making it difficult to separate both signals. However, for the other elements, it is possible to clearly differentiate regions 1 and 2. The green and magenta colors represent that the respective Tb and Ga elements are present on the crystals while three other figures (Ge, Pb and Bi) show that such elements are preferentially founded in the glassy phase, since in the crystal (region 2) there is an absence of these elements.

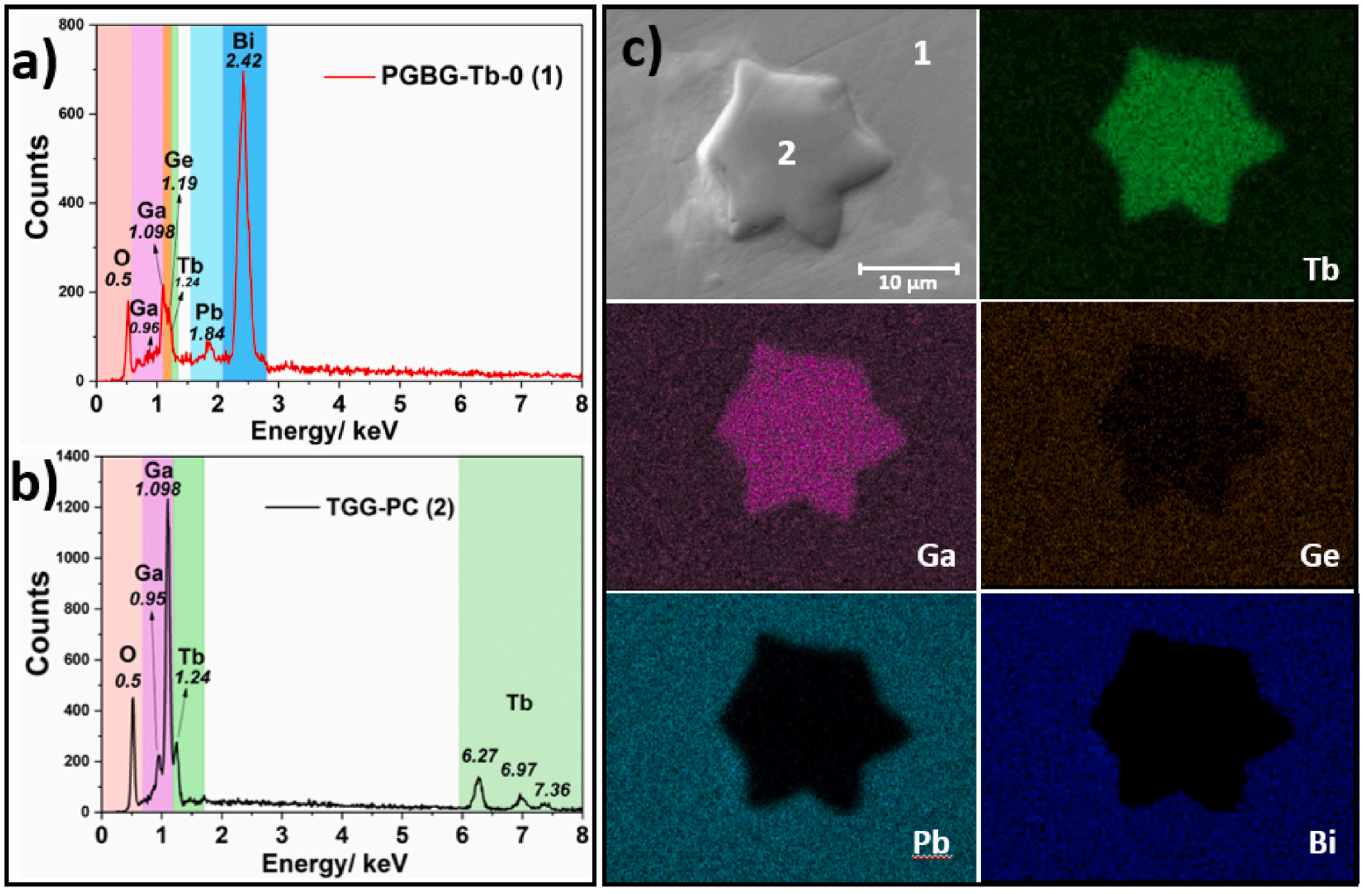

Fig. 3. **(a)** SEM-EDS spectrum of PGBG-Tb-O glass (point 1 in Figure c), **(b)** SEM-EDS spectrum of TGG crystal (point 2 in Figure c) and **(c)** SEM image and the respective elemental mapping results of each element for sample PGBG-Tb-0.

These results show that it is possible to use a heavy metal glass as reactor to obtain TGG-PC dispersed throughout the glass matrix. It is important to highlight that the crystals were formed in the bulk during pouring, without the need for any further thermal treatment. Furthermore, the data have indicated that with the increase in the time for crystal formation, it would be possible to obtain monocrystals and possibly larger crystals. For this reason, based on this set of data, a new strategy for the growth of these crystals has been implemented.

In this new approach, the PGBG-Tb vitreous precursors were melted at 1250 °C and then cooled inside the furnace at a rate of 10 °C/min until they reached 900 °C, during a total of 35 min and then, the crucible was removed from the furnace. Using this methodology, it was possible to obtain crystals between 50 μm and 100 μm with a perfect cubic shape (see Fig. 4a). This glass ceramic was immersed into concentrated nitric acid for 24 h and in this way, the vitreous part was dissolved, and the crystals could be recovered in large quantities and characterized. Fig. 4b shows a scanning electron microscopy image of one of the crystals obtained and extracted from the glass showing in detail the topography of the TGG-SC. In this scale, it is possible to observe that the acid does not attack the surface of the crystalline structure. This new methodology for obtaining TGG-SC opens a range of new applications in which these micro single crystals can be exploited, such as microleds.

The structural determination of the crystal was carried out using Single-crystal X-ray diffraction, which confirms that the synthesized minerals are composed of terbium gallium garnets single crystals (TGG-SC). The garnet crystallizes in the cubic system, with $a = 12.3539$ Å and space group $Ia\,\overline{3}\,d$, as expected for lanthanide gallium garnet [40]. The obtained crystal structure is depicted in Fig. 4c, in which it is possible to see the Tb^{3+} cations coordinated to eight oxygen atoms, and two independent units of Ga^{3+} cations, one of which is hexacoordinated in an octahedral geometry, while the other is tetracoordinated, in a tetrahedral geometry, with $\tau'_4 = 0.98$. The calculated distortion index (D) for Tb is 0.02017, while it is zero for the Ga atoms, highlighting the regularity of the coordination sphere. The quadratic elongation (<λ>) for the Ga atoms is of 1.0077 for the Ga hexacoordinated (Ga1) and 1.0148 for the tetracoordinated (Ga2). These parameters agree with those found for TGG structures from the ICSD database (coll. codes: 20831, 84875 and 184934), which present D value ranging from 0.01665 to 0.02174 for Tb and zero for Ga atoms, and <λ> between 1.0044 and 1.0102 for Ga1 and between 1.0105 and 1.0183 for Ga2. The Tb^{3+} cations are 3.783 Å from each other, while the separation between different Ga^{3+} atoms (Ga1–Ga2) is of 3.453 Å and between two tetracoordinated Ga atoms (Ga2–Ga2) is 3.783 Å. The values found for the similar structures in the database are in agreement with these values (Tb···Tb: 3.778–3.781 Å; Ga1-Ga2: 3.449–3.451 Å; Ga2-Ga2: 3.778–3.781 Å). Meanwhile, the distances Tb1–Ga1 and Tb1–Ga2 are 3.453 Å and 3.088 Å, respectively, and Ga1–Ga1 is 5.349 Å, also in agreement with the values taken from similar structures (Tb1-Ga1: 3.449–3.451 Å; Tb1-Ga2: 3.085–3.087 Å; Ga1-Ga1: 5.343–5.347 Å). A complete list of geometric parameters can be found in the Supplementary Material (Table S1).

In Fig. 4d it is possible to see the green emission arising from the TGG cubic crystals after excitation with a blue LED light (488 nm). As already explained, such emission comes from the $^5D_4 \rightarrow {}^7F_6$ transition of Tb^{3+} present into crystalline sites of the structure, as confirmed by the appearance of the Starks emissions observed in Fig. 4e. Even if the molar content of Tb^{3+} in the crystals would lead to quenching the emission, the luminescence of the crystals is intense enough under illumination of a weak LED of 488 nm source. Thus, the use of such crystals as green micro-LED′s is also promising.

The micro-Luminescence and micro-Raman mapping were obtained from the square surface of one crystal, and it is possible to observe the homogeneity of the luminescence and Raman spectra over the entire surface (Fig. 4f–g). Furthermore, the luminescence spectrum of the single crystal, (Fig. 4f), exhibits a higher definition of Tb^{3+} ion energy levels compared to the polycrystal (Fig. 2e). The Raman spectrum profile obtained for the TGG-SC, (Fig. 4g), also presents bands with higher definition than the TGG-PC shown in Fig. 2c, in addition, the TGG-SC spectrum is very similar to that of the commercial TGG obtained by Czochralski.

This data set presented in Fig. 4 shows the accuracy of the supersaturated solution methodology for obtaining TGG single crystals from the glass melt.

Finally, the magnetic properties of PGBG-Tb glasses were investigated by measurements of magnetic susceptibility in the temperature range from 5 to 300K. The ZFC molar magnetic susceptibilities of the glasses, as a function temperature (for samples obtained in different pouring times), were measured with an applied magnetic field of 100 Oe and the results are shown in Fig. 5a. The FC curves were not shown here, as they present the same behavior as the ZFC curve and are presented in the supplementary material (Fig. S3). Similar behavior was reported before and support the results [10].

The magnetic susceptibility vs. temperature curves of samples were fitted according to the Curie−Weiss Law, $\chi_M = C/T - \theta + \chi_0$, where C is the Curie constant, θ is the Weiss temperature and χ_0 represents the temperature-independent term, which is related to diamagnetic contribution. Negative θ values were obtained (see Table 2), indicating the presence of weak antiferromagnetic interactions between Tb^{3+} ions. As shown in Table 2, the absolute value of Weiss temperature increases with longer pouring time, suggesting that the antiferromagnetic interaction between terbium ions strengthens. This strongly indicates the formation of TGG crystals, supporting previous results. PGBG-Tb-0 sample contains fewer TGG crystals compared to the PGBG-Tb-4 sample and consequently, presents higher concentration of terbium ions into the glass matrix, leading to weaker antiferromagnetic interactions. Finally, it is important to highlight that the values obtained from the Curie-Weiss law fits from the $\chi_M \times T$ data are sufficiently close to zero, indicating the presence of paramagnetic behavior. Our results did not show a significant difference between the ZFC and FC measurements, indicating that the PGBG-Tb samples are not superparamagnetic and confirming that magnetic nanoclusters are not formed. In fact, all our findings point to the formation of bulk TGG structures.

The Curie constant depends on factors such as the number of magnetic domains (N), the Landé factor (g), the total angular momentum (J), the Boltzmann constant (k_b) and Bohr magneton (μ_b) [41,42]. The Curie constant values are resumed in Table 2. According to the data, a decrease in the Curie constant, as the pouring time increases, was observed. This behavior is directly related to the increase in the number of crystals, due to a greater number of magnetic domains, as well as due to the intensifying antiferromagnetic interactions between both Tb^{3+} ions in the glass matrix and in the crystals, corroborating to the observed decrease in the Curie constant.

Measurements of $M \times T$ curves (Fig. 5b) were obtained to determine the magnetic susceptibility of TGG crystals outside the glass matrix, within the temperature range from 5 to 300 K. TGG crystals with sizes ranging from 10 to 20 μm (TGG-PC) and from 50 to 70 μm (TGG-SC) were used to obtain these curves. The temperature-dependent magnetic susceptibility curves were fitted using the Curie-Weiss law, with the fits (red lines) shown in both Figures. The values extracted from these fits are presented in Table 2. The effective magnetic moment, μ_{eff}, was calculated using Curie constant as $\mu_{eff} = \sqrt{3k_bC/N_A\mu_B^2}$, where k_B is the Boltzmann's constant, N_A is the Avogadro's number, and μ_B is Bohr magneton. The calculated effective magnetic moment for Tb^{3+} ions was slightly lower than the theoretical value of 9.72 μ_B per Tb atom. In the same direction, the calculated μ_{eff} for Tb^{3+} ions was a little lower than the theoretical value in the glasses, except for the PGBG-Tb sample which contains low crystal concentration and for larger TGG-SC. The μ_{eff} values, systematically, decrease with increasing crystal size in the PGBG-Tb samples, deviating from the theoretical value. This behavior can be attributed to the partial quenching of angular momentum induced by

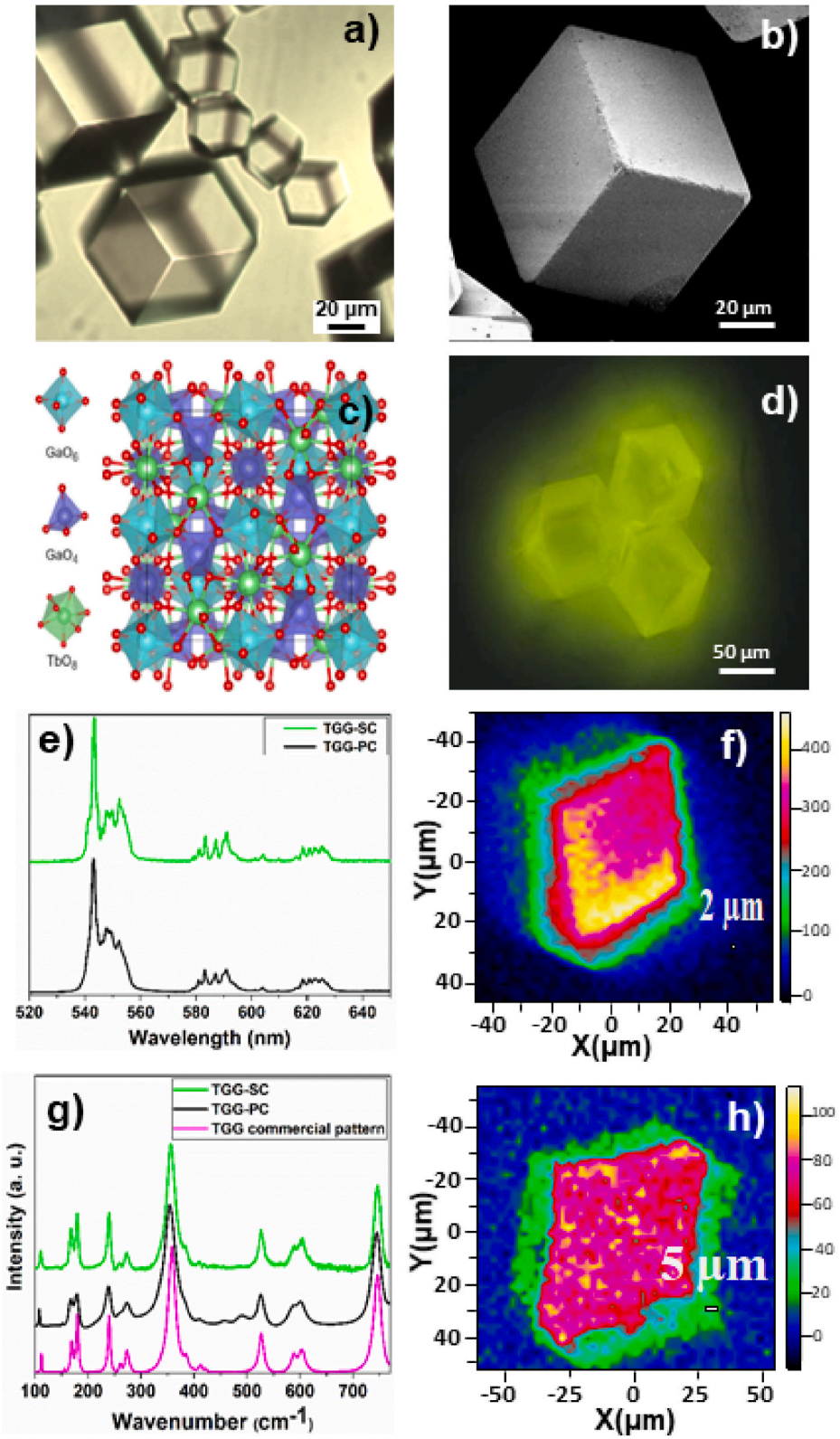

Fig. 4. **(a)** Optical microscopy image of TGG single crystals inside glass, **(b)** Scanning electron microscopy image of TGG-SC, **(c)** Crystal packing for TGG-SC obtained using the Vesta software, highlighting the TbO_8, GaO_6 and GaO_4 units, **(d)** Photograph of crystals under ultraviolet lamp, **(e)** Emission spectra acquired for TGG-SC, TGG-PC and TGG commercial pattern, **(f)** Luminescence map for emission bands between 530 and 560 nm, **(g)** Normalized Raman spectra acquired for TGG-SC, TGG-PC and TGG commercial pattern and **(h)** TGG-SC micro-Raman map for band at 356 cm^{-1}.

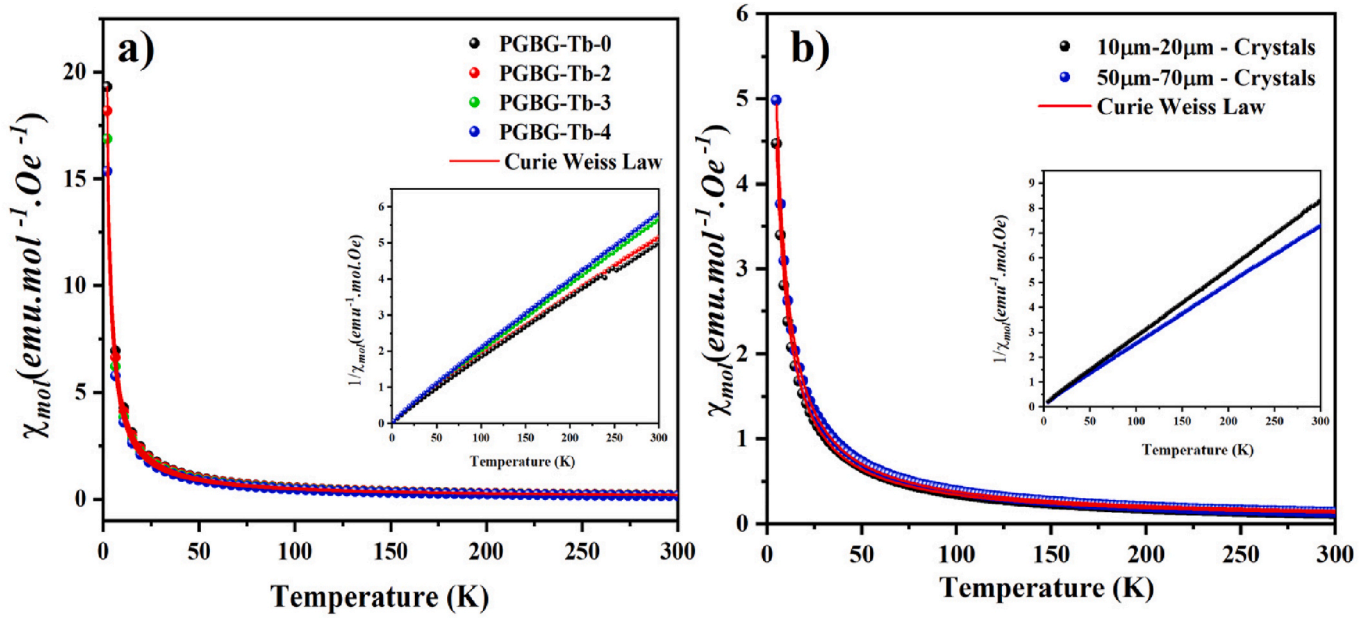

Fig. 5. **(a)** Temperature dependence (ZFC) of the magnetic susceptibility ($\chi_M \times T$) at 100 Oe for PGBG-Tb samples for different pouring times (the inset shows the temperature dependence of the inverse of the magnetic susceptibility ($1/\chi_M$)), **(b)** χ_M x T curves of TGG-PC (10–20 μm) and TGG-SC (50–70 μm), the inset shows the $1/\chi_M$ curves. The solid red lines, in both Figures represent the fit to the Curie-Weiss law. (For interpretation of the references to color in this figure legend, the reader is referred to the Web version of this article.)

Table 2
Parameters obtained by fitting the data with the Curie–Weiss law from 5 to 300 K.

Sample	C (emu K mol^{-1})	$\mu_{eff}(\mu_b)$	Θ(K)
PGBG - Tb0	47.7	9.7	−0.44
PGBG - Tb2	45.4	9.5	−0.50
PGBG - Tb3	42.7	9.3	−0.54
PGBG - Tb4	40.4	9.0	−0.64
Crystals (10–20 μm)	32.1	9.3	−2.29
Crystals (50–70 μm)	34.8	9.7	−2.12

the crystal field [43] and/or the competition between the magnetic moments of the Tb ions in the glass matrix and those within the crystals.

The Weiss temperature is negative for both crystal sizes, confirming that the interactions between the Tb crystals are antiferromagnetic. Notably, the results reveal that these antiferromagnetic interactions are stronger in pure TGG crystals than in those embedded within the glass matrix. Additionally, for crystals embedded in the glass, an increase in the absolute value of the Weiss temperature is observed, suggesting that crystal size influences the strength of the antiferromagnetic interactions. Additionally, XRD results showed that the crystals within these samples (PGBG-Tb samples) are polycrystalline, which could also contribute to this behavior. This enhancement of antiferromagnetic interactions with increasing crystal content can be explained by the progressive incorporation of Tb^{3+} ions into the well-ordered garnet lattice. In the TGG crystalline phase, the Tb^{3+} spins adopt a multiaxial AFA-type antiferromagnetic structure, with moments aligned along the ⟨100⟩ directions of the cubic unit cell and distributed across multiple sublattices [44,45]. This configuration arises from strong Ising-like anisotropy imposed by the crystal field and can be quantitatively understood using models based purely on dipolar interactions [46,47]. As the crystalline fraction increases, more Tb^{3+} ions participate in this network, reinforcing magnetic coupling and leading to more negative Weiss temperatures, as observed. These findings are consistent with prior studies of rare-earth garnets [43,46].

In Fig. 6(a–d) are shown the magnetization curves of the samples (PGBG-Tb, TGG_PC and TGG-SC) as a function of the applied dc magnetic field at 5 and 300 K. The magnetization nearly saturated under magnetic fields exceeding 60 kOe. No hysteresis loop was observed down to 5 K in any of the four PGBG-Tb samples, as expected, since paramagnetism is attributed to the Tb^{3+} ions. Instead, the isothermal magnetization curves display typical paramagnetic characteristics. Given this paramagnetic behavior, the Brillouin model can be applied, as described by the equations:

$$M = Ngj\mu_B B_{j(x)} \quad \text{eq. 1}$$

$$B_{j(x)} = \frac{2J+1}{2j} * coth - \frac{1}{2j} * \coth\left(\frac{1}{2j}x\right) \quad \text{eq. 2}$$

$$x = \frac{Jg\mu_B}{K(T+T_0)}H \quad \text{eq. 3}$$

Where M is magnetization per unit of mass, N is the number of magnetic ions per unit cell, g is the Landé factor, J is the total angular momentum, H is the magnetic field, and T_0 is a phenomenological parameter that represents any magnetic interaction that prevents spins from being completely aligned even in the strongest magnetic field [35]. It is known that the magnetic contribution of the TGG samples is due to the presence of Tb^{3+}, therefore we can define g = 1.5 and J = 6 [42]. The fits (red lines) present a good correlation with the experimental data, as shown in Fig. 6. According to Fig. 6a, an increase in saturation magnetization is observed with the increase in stirring time during the synthesis process of the PGBG samples. This can be attributed to the fact that a longer stirring time leads to an increase in both the number and size of crystals formed.

The crystals exhibit significantly higher saturation magnetization compared to those embedded in the glass matrix. Furthermore, larger crystals show a slight increase in saturation magnetization at both temperatures analyzed (300 K and 5 K). This behavior is also evidenced by the decrease in saturation magnetization as the size of the crystals in the glass matrix increases, as illustrated in the inset of Fig. 6c. The magnetic properties of crystals outside the glass matrix differ significantly from those within it. Pure crystals exhibit strong antiferromagnetic behavior, whereas this effect is reduced by approximately one order of magnitude in embedded crystals. Additionally, the

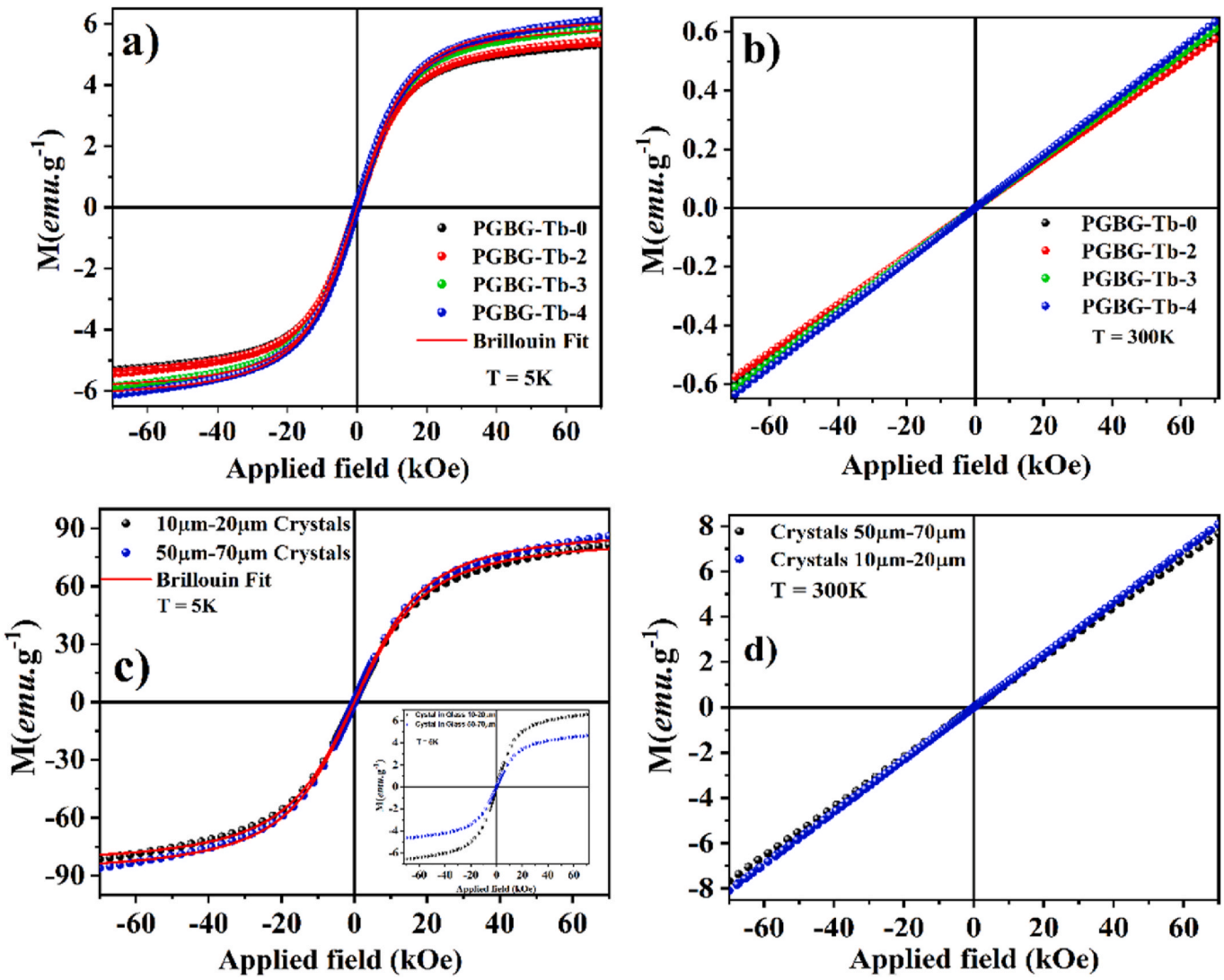

Fig. 6. Magnetization as a function of the applied magnetic field (M × H) is shown for **(a)** and **(b)** PGBG-Tb at 5 K and 300 K, respectively, and for **(c)** and **(d)** crystals extracted from the glass matrix at 5 K and 300 K, respectively. The inset of Figure (c) displays the M × H curves for crystals of sizes 10–20 μm and 50–70 μm embedded within the glass matrix.

magnetization curves of pure crystals show a saturation magnetization that is an order of magnitude higher than that of crystals incorporated into the glass matrix. This behavior aligns with experimental results for embedded crystals, which reveal a direct relationship between increased pouring time and enhanced antiferromagnetism, as evidenced by the Curie temperature and Curie constant analysis presented in Table 2. For the glass-embedded crystal samples, the saturation magnetization (Ms) values at 5 K were 5.25 emu/g (PGBG-Tb-0), 5.64 emu/g (PGBG-Tb-2), 5.76 emu/g (PGBG-Tb-3), and 6.01 emu/g (PGBG-Tb-4), corresponding to a relative increase of approximately 14.5 % from the shortest to the longest pouring time. This enhancement is attributed to the higher degree of crystallinity and the increasing number of magnetically active Tb^{3+} ions incorporated into the TGG phase. For the isolated crystals, the effect is even more pronounced. The Ms values reached 80.97 emu/g for crystals sized 10–20 μm and 86.92 emu/g for those sized 50–70 μm, reflecting the significantly higher concentration of ordered Tb^{3+} ions in the bulk crystalline state compared to the smaller embedded crystals within the glass matrix.

4. Conclusion

This paper reports the synthesis of terbium gallium garnets (TGG) from melted heavy metal oxide glass compositions without further thermal treatment. The adjustment of the cooling temperature allows obtaining poly and single crystalline phases of $Tb_3Ga_5O_{12}$ with different sizes. A chemical route was proposed to isolate the crystals from the parent glass without compromising their properties. Single-crystal X-ray diffraction confirmed the formation of the cubic phase with $Ia\,\bar{3}\,d$ space group for isolated single crystals. The luminescence results for both the glass-ceramics and the isolated crystals show the presence of well-defined Stark levels 543, 548 and 553 nm, indicating that the Tb^{3+} ions are in crystalline environments with a smaller number of symmetric sites and coherent with the Stark components of the TGG crystal. Crystals of medium size between 50 and 70 μm exhibit a magnetic behavior characteristic of antiferromagnetism, more pronounced in pure crystals than in those embedded in the glass matrix, which was corroborated by the Weiss temperature (2.12 K) and effective magnetic moment data (9.7 μB). This achievement represents an advance in the methodologies for obtaining magneto-optical TGG cubes in the micro-scale range, opening the possibility of mass production of such crystal and its uses in different technological applications.

CRediT authorship contribution statement

Juliane Resges Orives: Writing – original draft, Validation, Methodology, Investigation, Formal analysis, Conceptualization. **Thiago Augusto Lodi:** Investigation, Formal analysis. **Lia Mara Silva Marcondes:** Writing – review & editing, Writing – original draft, Investigation, Formal analysis, Conceptualization. **Camila Batista Pinto:** Investigation, Formal analysis. **Victória Mamelli:** Investigation, Formal analysis. **Antonio Eduardo Souza:** Writing – review & editing, Investigation. **Fabricio Benedito Destro:** Investigation, Formal analysis. **Juliani Caland:** Investigation, Formal analysis, Data curation. **Javier Alcides Ellena:** Writing – review & editing, Resources, Investigation. **Thierry Cardinal:** Writing – review & editing, Resources, Investigation. **Marc Dussauze:** Writing – review & editing, Resources, Investigation. **Jorlandio Felix:** Writing – review & editing, Resources, Investigation. **Marcelo Nalin:** Writing – review & editing, Writing – original draft, Supervision, Resources, Methodology, Conceptualization.

Declaration of competing interest

The authors whose names are listed immediately below certify that they have NO affiliations with or involvement in any organization or entity with any financial interest (such as honoraria; educational grants; participation in speakers' bureaus; membership, employment, consultancies, stock ownership, or other equity interest; and expert testimony or patent-licensing arrangements), or non-financial interest (such as personal or professional relationships, affiliations, knowledge or beliefs) in the subject matter or materials discussed in this manuscript.

Acknowledgments

The authors are grateful to the Brazilian funding agencies CNPQ and São Paulo Research Foundation FAPESP for the grants (2013/07793-6, 2019/19609-1, 2020/01786-1, 2023/09906-4, 2017/15850-0 e 2023/10889-7). J. F. Felix and J. Caland acknowledges Fundação de Apoio à Pesquisa do Distrito Federal (FAPDF, grant number: 193.00001823/2022-10 and 00193-00002418/2023-08) for financial support. All authors acknowledge Sisfóton by Ministry of Science, Technology and Innovation (MCTI), for research funding.

Appendix A. Supplementary data

Supplementary data to this article can be found online at https://doi.org/10.1016/j.ceramint.2025.08.137.

References

[1] H. Li, Y. Li, L. Zhang, E. Hu, D. Zhao, H. Guo, G. Qian, A thermo-responsive MOFs for X-Ray scintillator, Adv. Mater. 36 (2024), https://doi.org/10.1002/adma.202405535.

[2] W. Zhang, J. Wang, L. Wang, J. Wan, G. Bai, S. Xu, L. Chen, High-sensitivity ratiometric temperature sensing and information encryption based on upconversion emissions from lanthanide ions doped $BaTiO_3$ phosphor, Adv. Opt. Mater. 13 (2025), https://doi.org/10.1002/adom.202403290.

[3] X. Feng, S. Mou, Y. Pang, R. Long, C. Liu, Z. Bai, X. Liu, S. Liu, Lanthanide metal–organic frameworks with tunable fluorescence emission for sensing and photonic barcoding, Chem. Eng. J. 509 (2025), https://doi.org/10.1016/j.cej.2025.161474.

[4] Y. Li, J. Xu, T. Hu, G. Shi, Y. Peng, F. Qiao, L. Zhang, C. Zhao, Y. Kuang, L. Shen, Synthesis and Upconversion Luminescence fine-tuning of Yb^{3+}/Ho^{3+}-Doped indium and gallium oxide nanoparticles, Inorg. Chem. 63 (37) (2024) 17032–17042, https://doi.org/10.1021/acs.inorgchem.4c02701.

[5] S. Ahmad, Relativistic band structure engineering and optical-thermoelectric properties enhancement in Ho-doped Pr_2O_3 (1.25%, 2.5%): a DFT-based GGA+U+SOC first-principles study for next-generation PC-LEDs applications, J. Phys. Chem. Solid. 207 (2025), https://doi.org/10.1016/j.jpcs.2025.112943.

[6] S.C. Kaynar, A.S. Altowyan, H. Aydin, U.H. Kaynar, M.B. Coban, J. Hakami, N. Can, Judd–Ofelt analysis and photoluminescence behavior of Tb^{3+}-activated $K_7SrY_2(B_5O_{10})_3$ phosphors modified with alkali co-dopants for solid-state lighting applications, Spectrochim. Acta Mol. Biomol. Spectrosc. 341 (2025), https://doi.org/10.1016/j.saa.2025.126435.

[7] J. Xie, M. Zhang, H. Zeng, L. Zhang, H. Yu, H. Yuan, C. Ma, J. Hua, Y. Shi, Tb_2O_3/Ce_2O_3-Codoped B_2O_3-Ga_2O_3(Al_2O_3) glasses with a large faraday effect synthesized via containerless method for small optic isolators, ACS Appl. Mater. Interfaces 17 (2025) 14211–14219, https://doi.org/10.1021/acsami.4c20947.

[8] F. Unal, E. Yucel, Z.C. Orsel, M.F. Akyel, B. Ercan, Synthesis, characterization and cytocompatibility of Fe_3O_4@yttrium silicate: samarium nanoparticles with tunable magneto-luminescent properties, J. Alloys Compd. 1036 (2025), https://doi.org/10.1016/j.jallcom.2025.181885.

[9] D.F. Franco, Y. Ledemi, W. Correr, S. Morency, C.R.M. Afonso, S.H. Messaddeq, Y. Messaddeq, M. Nalin, Magneto-optical borogermanate glasses and fibers containing Tb^{3+}, Sci. Rep. 11 (2021) 1–16, https://doi.org/10.1038/s41598-021-89375-1.

[10] D.F. Franco, R.G. Fernandes, J.F. Felix, V.R. Mastelaro, H. Eckert, C.R.M. Afonso, Y. Messaddeq, S.H. Messaddeq, S. Morency, M. Nalin, Fundamental studies of magneto-optical borogermanate glasses and derived optical fibers containing Tb^{3+}, J. Mater. Res. Technol. 11 (2021) 312–327, https://doi.org/10.1016/j.jmrt.2021.01.010.

[11] W. Ming, Z. Jiang, G. Luo, Y. Xu, W. He, Z. Xie, D. Shen, L. Li, Progress in transparent nano-ceramics and their potential applications, Nanomaterials 12 (9) (2022) 1491, https://doi.org/10.3390/nano12091491.

[12] D. Franta, M.G. Mureşan, P. Ondračka, B. Hroncová, F. Vižďa, Wide spectral range optical characterization of terbium gallium garnet (TGG) single crystal by universal dispersion model, Opt. Laser Technol. 181 (2025), https://doi.org/10.1016/j.optlastec.2024.111916.

[13] M. Watanabe, Y. Anzai, I. Tanaka, Characterization of defects in $Tb_3Ga_5O_{12}$ single crystals grown by the Czochralski method, J. Cryst. Growth 634 (2024), https://doi.org/10.1016/j.jcrysgro.2024.127687.

[14] L.V. Albino, M. Dussauze, O. Toulemonde, M. Duttine, V. Jubera, D.F. Franco, T. Cardinal, M. Nalin, Paramagnetic borotungstate glasses with high terbium concentration for magneto-optical applications, J. Non-Cryst. Solids 627 (2024), https://doi.org/10.1016/j.jnoncrysol.2023.122811.

[15] D.F. Franco, F.J. Caixeta, L.V. Albino, T.A. Lodi, J.R. Orives, E.O. Ghezzi, M. Nalin, Terbium-doped transparent glass-ceramics containing $TbPO_4$ crystals: a promising material for photonic applications, Opt. Mater. X 20 (2023), https://doi.org/10.1016/j.omx.2023.100272.

[16] X. Li, Q. Liu, H. Pan, N. Jiang, Z. Yang, T. Xie, L. Wu, J. Li, Transparent $Tb_3Ga_5O_{12}$ magneto-optical ceramics sintered from co-precipitated nano-powders calcined at different temperatures, Opt. Mater. 90 (2019) 26–32, https://doi.org/10.1016/j.optmat.2019.02.009.

[17] X. Li, L. Zhang, T. Li, C. Hu, H. Hao, L. Wu, D. Hreniak, J. Li, Effect of non-stoichiometric Ga content on the microstructure and optical transparency of terbium gallium garnet ceramics, Opt. Mater. 154 (2024), https://doi.org/10.1016/j.optmat.2024.115648.

[18] Z. Chen, L. Zhu, J. Yi, C. Yang, Fabrication and characterization of a gadolinium-doped terbium gallium garnet crystal with an enhanced Verdet constant, Opt. Lett. 47 (2022) 2270, https://doi.org/10.1364/ol.457086.

[19] Y. Onishi, T. Nakamura, H. Sone, S. Adachi, Synthesis and properties of $Tb_3Al_5O_{12}$:Eu^{3+} garnet phosphor, J. Lumin. 197 (2018) 242–247, https://doi.org/10.1016/j.jlumin.2018.01.043.

[20] V.I. Chani, A. Yoshikawa, H. Machida, T. Satoh, T. Fukuda, Growth of $Tb_3Ga_5O_{12}$ fiber and bulk crystals using micro-pulling-down apparatus, J. Cryst. Growth 210 (2000) 663–669.

[21] Z. Chen, L. Yang, X. Wang, J. Wang, Y. Hang, Highly transparent terbium gallium garnet crystal fabricated by the floating zone method for visible-infrared optical isolators, Opt. Mater. 46 (2015) 12–15, https://doi.org/10.1016/j.optmat.2015.03.034.

[22] M. Watanabe, Y. Maruyama, K. Nagao, Y. Anzai, M. Nagao, S. Watauchi, I. Tanaka, Czochralski growth and composition control of $Tb_3Ga_5O_{12}$ single crystals, J. Cryst. Growth 665 (2025), https://doi.org/10.1016/j.jcrysgro.2025.128205.

[23] C. Zhe, Z. Ling, Y. Yong, Y. Chao, Enhancement of magneto-optical performance of $Tb_{2.85}Er_{0.15}Ga_5O_{12}$ crystal with high transmittance, Opt. Mater. 128 (2022) 112354, https://doi.org/10.1016/j.optmat.2022.112354.

[24] X. Xin, Y. Hao, X. Yang, Z. Zhang, Q. Hu, X. Fu, Z. Jia, X. Tao, Research on the magneto-optical performance of Gd^{3+} doped $Tb_3Al_3Ga_2O_{12}$ crystal, Opt. Mater. 159 (2025) 116640, https://doi.org/10.1016/j.optmat.2024.116640.

[25] T. Chen, Y. Yu, L. Li, J. Zhu, M. Cong, J. Song, Eliminate of colour center and growth of large-size $Tb_3Ga_5O_{12}$ crystals, J. Cryst. Growth 562 (2021), https://doi.org/10.1016/j.jcrysgro.2021.126090.

[26] M. Nalin, L.V. Albino, T.A. Lodi, J.R. Orives, L.M. Marcondes, A.A. Habib, M.H. R. Acosta, E.D. Zanotto, D.F. Franco, Novel scalable synthesis of luminescent and magnetic single crystal garnets, Mater. Horiz. (2025), https://doi.org/10.1039/d5mh00254k.

[27] M. Yamane, Y. Asahara, Glasses for Photonics, 1a Edition, 2000. http://journal.um-surabaya.ac.id/index.php/JKM/article/view/2203.

[28] E.D. Zanotto, J.C. Mauro, The glassy state of matter: its definition and ultimate fate, J. Non-Cryst. Solids 471 (2017) 490–495, https://doi.org/10.1016/j.jnoncrysol.2017.05.019.

[29] L.M. Marcondes, R.O. Evangelista, R.R. Gonçalves, A.S.S. de Camargo, D. Manzani, M. Nalin, F.C. Cassanjes, G.Y. Poirier, Er^{3+}-doped niobium alkali germanate glasses and glass-ceramics: NIR and visible luminescence properties, J. Non-Cryst. Solids 521 (2019), https://doi.org/10.1016/j.jnoncrysol.2019.119492.

[30] A.E. Souza, S.G. Antonio, S.J.L. Ribeiro, D.F. Franco, G. Galeani, T. Cardinal, M. Dussauze, M. Nalin, Heavy metal oxide glass-ceramics containing luminescent gallium-garnets single crystals for photonic applications, J. Alloys Compd. 864 (2021), https://doi.org/10.1016/j.jallcom.2021.158804.

[31] A.S. Myerson, D. Erdemir, A.Y. Lee, Handbook of Industrial Crystallization, third ed., Cambridge University Press, 2019.
[32] O.V. Dolomanov, L.J. Bourhis, R.J. Gildea, J.A.K. Howard, H. Puschmann, OLEX2: a complete structure solution, refinement and analysis program, J. Appl. Crystallogr. 42 (2009) 339–341, https://doi.org/10.1107/S0021889808042726.
[33] K. Momma, F. Izumi, VESTA 3 for three-dimensional visualization of crystal, volumetric and morphology data, J. Appl. Crystallogr. 44 (2011) 1272–1276, https://doi.org/10.1107/S0021889811038970.
[34] A.D. Sontakke, K. Biswas, K. Annapurna, Concentration-dependent luminescence of Tb^{3+} ions in high calcium aluminosilicate glasses, J. Lumin. 129 (2009) 1347–1355, https://doi.org/10.1016/j.jlumin.2009.06.027.
[35] O.L. Malta, L.D. Carlos, Intensities of 4f-4f transitions in glass materials, Quim. Nova 26 (2003) 889–895, https://doi.org/10.1590/S0100-40422003000600018.
[36] M. Montesso, D. Manzani, J.P. Donoso, C.J. Magon, I.D.A. Silva, M. Chiesa, E. Morra, M. Nalin, Synthesis and structural characterization of a new $SbPO_4$-GeO_2 glass system, J. Non-Cryst. Solids 500 (2018) 133–140, https://doi.org/10.1016/j.jnoncrysol.2018.07.005.
[37] T. Guérineau, C. Strutynski, T. Skopak, S. Morency, A. Hanafi, F. Calzavara, Y. Ledemi, S. Danto, T. Cardinal, Y. Messaddeq, E. Fargin, Extended germano-gallate fiber drawing domain: from germanates to gallates optical fibers, Opt. Mater. Express 9 (2019) 2437, https://doi.org/10.1364/ome.9.002437.
[38] K. Sawada, T. Nakamura, S. Adachi, Europium gallium garnet ($Eu_3Ga_5O_{12}$) and Eu_3GaO_6: synthesis and material properties, J. Appl. Phys. 120 (2016), https://doi.org/10.1063/1.4964444.
[39] R.C. Middleton, D.V.S. Muthu, M.B. Kruger, High-pressure spectroscopic studies of europium gallium and gadolinium aluminum garnets, Solid State Commun. 148 (2008) 310–313, https://doi.org/10.1016/j.ssc.2008.09.002.
[40] V. Monteseguro, P. Rodríguez-Hernández, R. Vilaplana, F.J. Manjón, V. Venkatramu, D. Errandonea, V. Lavín, A. Muñoz, Lattice dynamics study of nanocrystalline yttrium gallium garnet at high pressure, J. Phys. Chem. C 118 (2014) 13177–13185, https://doi.org/10.1021/jp501570c.
[41] E.J.F. Conceição, F.F.H. Aragón, Y.A. Urian, T.J. Castro, J.A.H. Coaquira, P. C. Morais, S.W. da Silva, Effects of Gd doping on the structural, optical and magnetic properties of $Ce_{1-x}Gd_xO_{2-\delta}$ nanoparticles and the impact of the oxygen vacancy, J. Alloys Compd. 960 (2023), https://doi.org/10.1016/j.jallcom.2023.170628.
[42] L.V. Albino, N.G. Roque, L.M. Marcondes, J.R. Orives, D.F. Franco, R.S. Manzan, F. H. Aragón, J.F. Felix, M. Nalin, Magnetic and magneto-optical properties of manganese-containing antimony phosphate glasses – an alternative to Faraday rotators, Opt. Mater. 147 (2024), https://doi.org/10.1016/j.optmat.2023.114674.
[43] P. Mukherjee, A.C. Sackville Hamilton, H.F.J. Glass, S.E. Dutton, Sensitivity of magnetic properties to chemical pressure in lanthanide garnets $Ln_3A_2X_3O_{12}$, Ln = Gd, Tb, Dy, Ho, A = Ga, Sc, In, Te, X = Ga, Al, Li, J. Phys. Condens. Matter 29 (2017), https://doi.org/10.1088/1361-648X/aa810e.
[44] R. Wawrzyńczak, B. Tomasello, P. Manuel, D. Khalyavin, M.D. Le, T. Guidi, A. Cervellino, T. Ziman, M. Boehm, G.J. Nilsen, T. Fennell, Magnetic order and single-ion anisotropy in $Tb_3Ga_5O_{12}$, Phys. Rev. B 100 (2019) 094442, https://doi.org/10.1103/PhysRevB.100.094442.
[45] S. Petit, F. Damay, Q. Berrod, J.M. Zanotti, Spin and lattice dynamics in the two-singlet system $Tb_3Ga_5O_{12}$, Phys. Rev. Res. 3 (2021) 013030, https://doi.org/10.1103/PhysRevResearch.3.013030.
[46] H.W. Capel, Magnetic properties of rare earth ions in aluminium and gallium garnets, Physica 31 (1965) 570, https://doi.org/10.1016/0031-8914(65)90160-6.
[47] I.A. Kibalin, F. Damay, X. Fabrèges, A. Gukassov, S. Petit, Competing interactions in dysprosium garnets and generalized magnetic phase diagram of S= 1/2 spins on a hyperkagome network, Phys. Rev. Res. 2 (2020) 033509, https://doi.org/10.1103/PhysRevResearch.2.033509.